Physics of Fluids

RESEARCH ARTICLE | NOVEMBER 21 2023

Laser-induced, single droplet fragmentation dynamics revealed through megahertz x-ray microscopy

Fabian Reuter ; Tokushi Sato (佐藤篤志) ; Valerio Bellucci ; Sarlota Birnsteinova ; Carsten Deiter ; Jayanath C. P. Koliyadu ; Romain Letrun ; Pablo Villanueva-Perez ; Richard Bean ; Adrian P. Mancuso ; Alke Meents ; Patrik Vagovic ; Claus-Dieter Ohl

Physics of Fluids 35, 113323 (2023)
https://doi.org/10.1063/5.0171225

Physics of Fluids ARTICLE pubs.aip.org/aip/pof

Laser-induced, single droplet fragmentation dynamics revealed through megahertz x-ray microscopy

Cite as: Phys. Fluids **35**, 113323 (2023); doi: 10.1063/5.0171225
Submitted: 7 August 2023 · Accepted: 26 October 2023 ·
Published Online: 21 November 2023

Fabian Reuter,[1,2,a)] Tokushi Sato, (佐藤篤志)[1] Valerio Bellucci,[1] Sarlota Birnsteinova,[1] Carsten Deiter,[1] Jayanath C. P. Koliyadu,[1] Romain Letrun,[1] Pablo Villanueva-Perez,[3] Richard Bean,[1] Adrian P. Mancuso,[1,4] Alke Meents,[5] Patrik Vagovic,[1,5] and Claus-Dieter Ohl[6]

AFFILIATIONS

[1]Faculty of Natural Sciences, Institute for Physics, Otto von Guericke University Magdeburg, Universitätsplatz 2, 39106 Magdeburg, Germany
[2]European XFEL GmbH–The European X-Ray Free-Electron Laser, Schenefeld, Germany
[3]Synchrotron Radiation Research and NanoLund, Lund University, Lund, Sweden
[4]Diamond Light Source Ltd., Harwell Science and Innovation Campus, Didcot OX11 0DE, United Kingdom and Department of Chemistry and Physics, La Trobe Institute for Molecular Science, La Trobe University, Melbourne, Victoria 3086, Australia
[5]Center for Free-Electron Laser Science (CFEL), DESY, Hamburg, Germany
[6]Faculty of Natural Sciences, Institute for Physics, Otto von Guericke University Magdeburg, Universitätsplatz 2, 39106 Magdeburg, Germany

[a)]Author to whom correspondence should be addressed: Fabian.Reuter@ovgu.de

ABSTRACT

The fragmentation dynamics of single water droplets from laser irradiation is studied with megahertz frame rate x-ray microscopy. Owed to the nearly refraction-free and penetrating imaging technique, we could look into the interior of the droplet and reveal that two mechanisms are responsible for the initial explosive fragmentation of the droplet. First, reflection and diffraction of the laser beam at the droplet interface result in the formation of laser ray caustics that lead to non-homogeneous heating of the droplet, locally above the critical temperature. Second, homogeneous cavitation in the droplet that is likely caused from shockwaves reflected as tension waves at the acoustic soft boundaries of the droplet. Further atomization occurs in three stages, first a fine sub-micrometer sized mist forms on the side of the droplet posterior to laser incidence, then micrometer sized droplets are expelled from the rim of an expanding liquid sheet, and finally into droplets of larger size through hole and ligament formation in the thinning liquid sheet where ligaments pinch off.

I. INTRODUCTION

Atomization is the process of fragmenting larger liquid masses into smaller droplets and fine sprays.[1] It may be desirable in industrial and medical applications, yet it also could be undesired in modern liquid droplet shaping.[2] In many of the processes resulting in droplet atomization, shock waves interact either externally with the droplet[3] or are created within. For example, the impact of rain on fast-moving planes and trains results in shock and expansion waves that once launched within the droplet may atomize the droplet by overcoming the yield strength of the liquid. In particular, expansion waves formed upon an acoustic soft reflection of shock waves may cause a vapor phase explosion within the droplet.[4]

In addition to the droplet impact, pressure waves may be generated with pulsed lasers[5–8] or x-ray illumination.[9] When the liquid is opaque to the radiation, momentum can be transferred through the vaporization of a thin layer of liquid, thus propelling and deforming the liquid sphere into a thin and radially expanding sheet.[2,10,11] At higher laser intensities within nontransparent droplets, shocks may be launched that result in spallation and cavitation within the droplet.[12–17] In less-absorbing liquids, this phase transition may be initiated

through an optical breakdown, resulting in an explosively expanding vapor bubble that also launches shock waves. The complexity of the droplet atomization is caused by the interaction of the shock waves and cavitation bubbles with the liquid–gas interface, giving rise to Rayleigh–Taylor instabilities,[18] spallation, and secondary cavitation. A technical application is the shaping of droplets into thin sheets, which is a prerequisite for the generation of extreme UV light. This is currently done through pulsed laser illumination of liquid tin droplets. With increasing laser intensities or smaller droplet sizes, the droplet may not form a sheet but grows in volume and develops radially outward pointing jets on its surface; both features are driven by expanding cavitation bubbles within the droplet. Yet it is not clear where the phase transition occurs. Even in a surrogate liquid such as water, the small size of the droplet prevents a look into the complex fluid dynamics at very short time scales when using visible light.

The time-resolved MHz x-ray microscopy developed at European XFEL[19] used here overcomes these limitations. In particular, the nearly refraction-free illumination offers a view into the droplet and also has a nearly infinite depth of field to resolve the three-dimensional fragmentation dynamics.

II. EXPERIMENTAL SETUP

A sketch of the droplet generation and laser-fragmentation setup is given in Fig. 1 (bottom). A single, sub-millimeter-sized droplet of de-ionized water was acoustically levitated in air. The beam of a pulsed laser (wavelength: 1030 nm, pulse energy attenuated to 1 mJ, pulse duration 850 fs, and spot size FWHM 350 μm; laser developed at European XFEL facility[20,21]) was made slightly convergent with a lens located close to the droplet (focal length $f = 750$ mm) and aligned to completely illuminate the droplet from one side. As the droplet was hit by the laser, a rapid phase explosion fragmented the droplet. The fragmentation dynamics was recorded with the MHz x-ray microscopy setup developed within an internal R&D project of European XFEL, based on an indirect x-ray detector, a fast scintillator, a diffraction limited optical microscope with near ultraviolet (NUV) optics, and two megahertz cameras Shimadzu HPV-X2. A magnification was obtained with a 10× objective (Mitutoyo long working distance objective, 10×, NUV, 0.28 NA) resulting in an effective pixel size of 3.2 μm. The x-ray pulse repetition rate is 1.125 MHz, and both high-speed cameras are synchronized to the x-ray pulses to record one image per x-ray pulse. Additionally, the cameras are aligned back to back in time, extending the image buffer to 256 frames at full spatial resolution instead of the 128 frames for a single camera. The schematic configuration of the experiment is sketched in Fig. 1 (top).

An avalanche photodiode was used to measure the instance of laser pulse impact on the droplet with respect to the first frame of the imaging series where the uncertainty is estimated to be below 1 ns, which results from the uncertainty of the distance between droplet and photodiode and the finite speed of light.

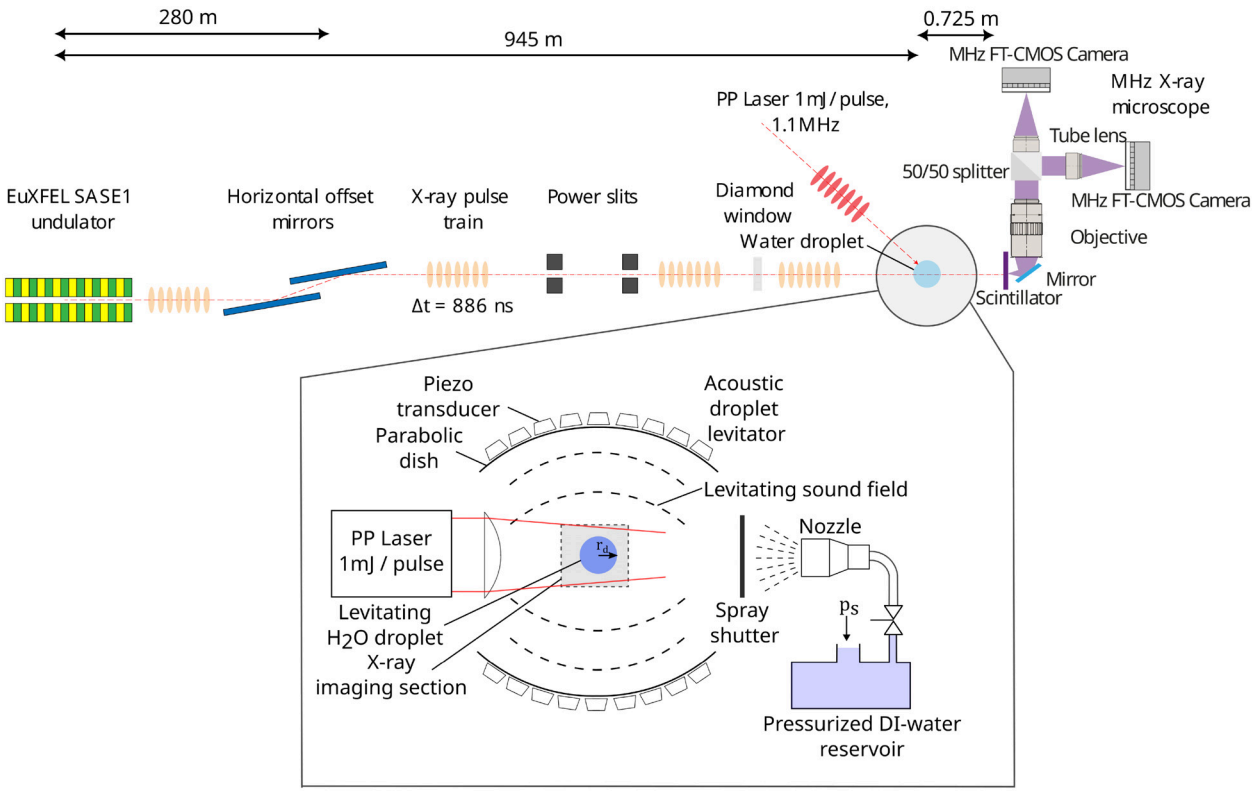

FIG. 1. Schematics of experimental arrangement with direct beam illumination at SPB/SFX instrument at EuXFEL (top) and sample setup (bottom). A water spray is produced through a nozzle, and a water droplet (of a specific size) is trapped in the standing wave field of the acoustic levitator. A mildly convergent laser pulse explosively fragments the quiescent droplet. The time-resolved dynamics are recorded in the x-ray imaging section.

To study a symmetric and unbounded droplet, a single droplet was trapped in an in-house built acoustic levitator based on the TinyLev design.[22] It consists of two spherical caps, each equipped with 36 piezoelectric transducers. The spherical caps are mounted at a distance of ≈ 125 mm to form a standing wave when driven at 80 kHz. Electric driving powers were set between 5 and 15 W allowing to trap droplets with a final radius r_d between ≈40 and ≈80 μm. These parameters allow the trapping of spherical droplets that do not show oscillations in the sound field. From the spray, a single droplet was acoustically trapped and levitated along the axis of cylindrical symmetry near the center of the levitator. The droplet generation and trapping had to be automatized, as physical access to the setup was limited during beam time. Therefore, a simple and robust remote solution of droplet generation was found by first producing a spray of fine droplets, from which then individual droplets at various pressure nodes are trapped. The spray naturally contains a broad range of combinations of droplet sizes, velocities, and injection positions with respect to the acoustic field. Thus, the necessary conditions for droplet trapping are met in some cases without the requirement for fine-tuning or readjustment of experimental parameters during the test runs. This is further discussed in Appendix A, where also a microscopic high-speed video of the spray passing through the sound field and the trapping of droplets is provided (Fig. 8, Multimedia view). A short spray burst was generated from de-ionized water through a nozzle of diameter ≈315 μm. The de-ionized water was filled into a pressurized reservoir with a gauge pressure of $p_s \approx 2.5$ bar connected to an air supply line. The burst duration was about 150 ms controlled with a magnetic valve. Due to the finite opening time of the valve and the elasticity of the tubing, the spray needed some time to develop, i.e., reach the desired fine droplet sizes and large velocities in the spray. Therefore, a servo-driven mechanical shutter was employed about 2 cm in front of the nozzle exit that unblocked the spray for about 30 ms only once the spray had fully formed. After a few seconds, once the droplet was quiescently trapped, the measurement started with the firing of the laser pulse and triggering of the x-ray high-speed imaging. The remote control of the repeated droplet generation was conducted with a microcontroller that controls the magnetic valve and the mechanical shutter.

A. Image processing and droplet tracking

All images are pre-processed in the following way: a high-pass Fourier filter (cutoff wavelength 80 pixels) is used to remove vertical and horizontal stripes from the x-ray background illumination. Then, a flat-field correction is employed, where the flat field image is obtained from the median intensity of the entire time series. As the brightness varied between each x-ray pulse in the pulse train, the intensity in each frame is further normalized to its background brightness. The background brightness is measured via a Gaussian fit to the main peak in the intensity histogram of each frame using MATLAB. This gives uniform contrast throughout each image and the entire imaging series, necessary to automatically track droplets between frames. The tracking is achieved using the TrackMate Plugin[23] in Fiji. Droplets are identified using the threshold detector and linked in time using the "Kalman" tracker. The intensity along the droplet boundary is resolved using a cubic fitting to achieve some sub-pixel accuracy, and the radius is estimated from the droplet area. We estimate the accuracy to be of half a pixel. Each identified droplet typically contains more than ten measurements in ten subsequent frames resulting in an uncertainty in droplet radius of 0.5 μm. Droplet velocities are calculated from the difference between start and end point along one path and divided by the total frame time. The frame time error is negligible, and the uncertainty stems from the expected error in droplet localization. With a localization error of a droplet center of half a pixel, one obtains an uncertainty of 0.17 m/s. For illustration, the video sequence with tracked droplets is shown in Fig. 9 (Multimedia view). The tracking data are exported to MATLAB and filtered to exclude objects that are not correctly detected droplets for which the following criteria are used. Not reliably and consistently detected objects are excluded, i.e., objects that are detected in too few frames. Objects with too large radius variations over time, as these likely stem from droplets incorrectly linked in time, are excluded. Objects with too little circularity, mainly caused by detecting liquid filaments instead of spherical droplets, are excluded.

B. Numerical modeling

To reveal the temperature distribution of the droplet interior, a laser-induced heating is modeled using COMSOL Multiphysics for a spherical water droplet of radius $r_d = 75$ μm in cylindrical symmetry. Therefore, the COMSOL ray tracing module is coupled with the heat transfer from the solid module, which is applicable to the liquid here, as the timescale of heat convection is much longer than the time of heating, i.e., the laser pulse duration is less than $\tau_l = 1$ ps. The timescale of thermal convection can be estimated as $\tau_c = \frac{\eta}{\rho\beta\Delta T r_d g}$, with the mass density of water $\rho = 1000\,\mathrm{kg\,m^3}$, the thermal expansion coefficient $\beta = 0.000\,214\ \mathrm{K^{-1}}$, the temperature difference between room temperature and the critical temperature of water $\Delta T = 354$ K, the gravity acceleration $g = 9.81\,\mathrm{m\,s^{-2}}$, and the dynamic viscosity of water $\eta = 0.000\,89$ Pa s. Then, $\frac{\tau_l}{\tau_c} = \frac{1\,\mathrm{ps}}{16\,\mathrm{ms}} = 6.25 \times 10^{-11}$, i.e., heat convection is negligible here. Similarly, thermal diffusion can be neglected here as its characteristic timescale is $\tau_d = r_d^2/\alpha = 38.5$ ms, where $\alpha = 0.146\,\mathrm{mm^2\,s^{-1}}$ is the thermal diffusivity of water, i.e., $\frac{\tau_l}{\tau_c} = 2.6 \times 10^{-11}$. As the droplet diameter $2r_d$ is much smaller than the laser beam diameter (FWHM laser beam: ≈ 350 μm), the beam intensity can be considered homogeneous across the droplet cross section. Consequently, the laser rays causing the heating are approximated with parallel rays of uniform intensity hitting the droplet with an initial uniform temperature of 293 K (room temperature). The locally absorbed laser power is proportional to the ray power and given via the imaginary part of the optic refractive index of water at the wavelength of 1030 nm, i.e., $\Im(n) = 3.2 \times 10^6$. The variation of the refractive index with temperature is neglected, as the thermo-optic coefficient of water in the relevant range is rather small: $\partial n/\partial T \approx -1.5 \times 10^{-5}\ \mathrm{K^{-1}}$, see Ref. 24.

III. RESULTS

Figure 2 presents the early laser-induced fragmentation dynamics recorded with x-ray imaging. It is a composite image from three different droplets recorded at different time delays with respect to the laser to virtually increase the temporal resolution beyond the framing rate of 1.125 MHz. We evaluated the fragmentation dynamics for droplet sizes between $r_d \approx 40$ and $r_d = 81$ μm. Within this size range, the droplet fragmentation qualitatively shows the same dynamics, which was confirmed visually. The droplet appears dark due to the x-ray absorption, with a bright fringe caused by a phase contrast, which is a

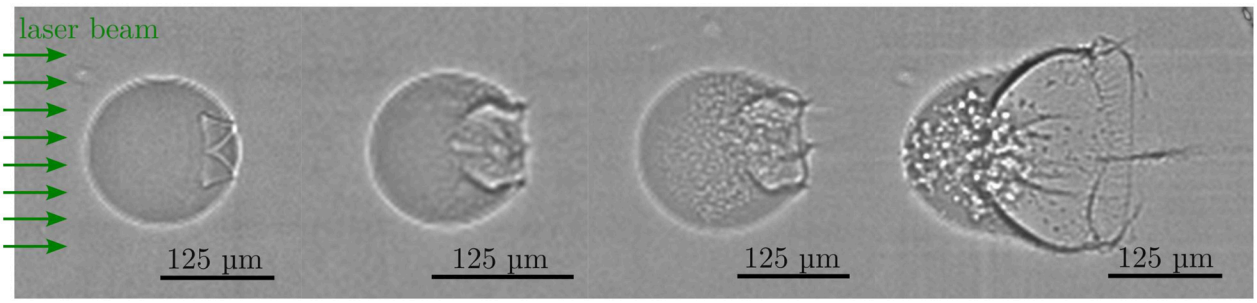

FIG. 2. Initial dynamics of the exploding droplet. To achieve an increased temporal resolution, two frames from similar droplets imaged at different delays with respect to the heating laser pulse are inserted in between the first and the last frame. The time delays with respect to the laser for the four frames are 18.5, 92.5, 185, and 907 ns. Images are scaled in size to ease comparison, as r_d differs between the experiments [note the different scale bars, from left to right: $r_d = 80,\ 62,\ 81,$ and 80 μm ($\pm 2.5\ \mu$m)]. The laser beam is incident from the left.

result of the difference in refractive index between water and air in combination with the coherent x-ray illumination.[25,26]

A mass density variation from superheated and potentially evaporated water is visible in the droplet sphere posterior to the laser incidence. From here, a phase explosion leading to the droplet fragmentation is initiated. In the second frame, $t = 92.5$ ns a cavity has formed that will rupture to the atmosphere. In addition, the droplet surface appears rough and at $t = 185$ ns many small vapor cavities in the droplet are expanding. Vapor bubbles can be nucleated either thermally or mechanically, i.e., from low pressures. Below we will show that bubbles are also similarly nucleated where temperatures are clearly below the boiling point of water. Here, we could not directly observe shockwaves. However, earlier work has shown that laser-induced heat deposition resulting in a phase explosion launches shock waves.[27] A shockwave traveling within a droplet is reflected at the water–air interface with a phase jump, i.e., the leading positive pressure pulse of the shock front is converted into a tensile pulse as the acoustic impedance of water is much larger than that of air.[28] This tensile phase can induce cavitation nucleation within the droplet.[3,17] Around $t = 4R/c = 150\ \mu\text{m}/1483\ \text{ms}^{-1} = 200$ ns, where $c = 1483\ \text{ms}^{-1}$, i.e., roughly in the third frame $t = 185$ ns, the reflected shockwave must have passed through the entire droplet. Here, density fluctuations are also seen within the intact left side of the droplet they grow into the bigger bubbles shown in the fourth frame connect with the right cavity and start ejecting droplets into the atmosphere. As the time of bubble nucleation is consistent with the time of bubble nucleation and thermal effects can be excluded at this timescale (see below), we conclude that the reflected shockwave is responsible for the vast bubble nucleation within the droplet.

The subsequent dynamics are shown in Fig. 3. They occur on a longer timescale; thus, the presented frames are selected from a single droplet experiment. The main cavity formed by the phase explosion expands, while the remaining left part of the droplet is ejected to the left of the frame. The secondary cavitation bubbles in the remaining droplet are collapsed around $t = 3.6\ \mu$s. This short lifetime is known for cavitation bubbles driven by a constant static pressure of 1 bar from a maximum radius of $R_{max} = 20\ \mu$m. This size is in agreement with the sizes of bubbles found in Fig. 3 at $t = 1.8\ \mu$s.

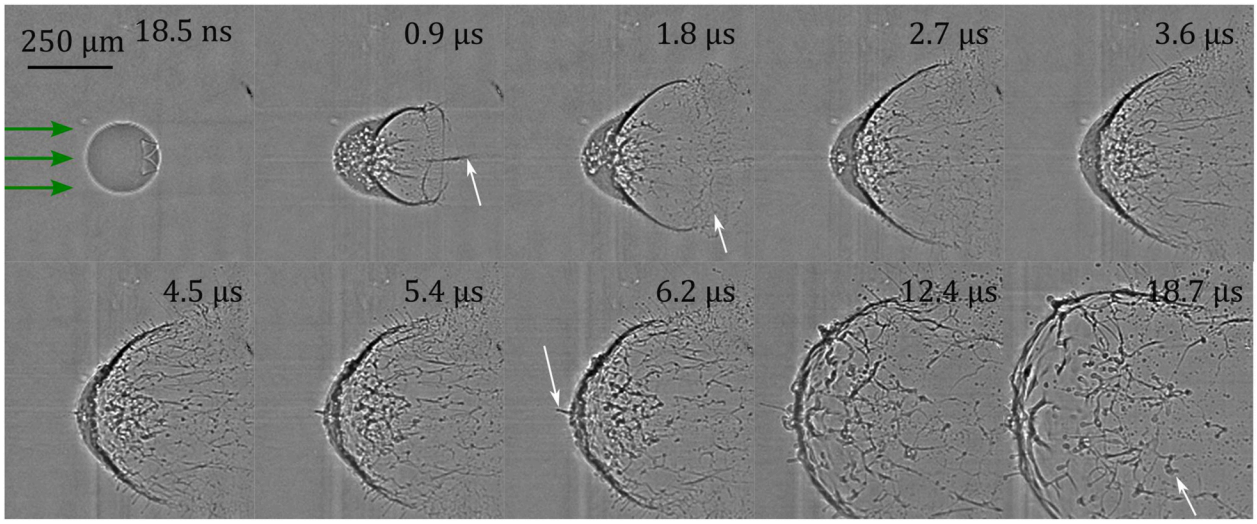

FIG. 3. X-ray imaging of laser-induced fragmentation dynamics of a single water droplet levitated in the acoustic trap. The arrows in the first frame indicates the direction of the incident laser beam. Times in each frame are given with respect to the fragmenting laser pulse.

An interesting detail is the formation of a thin liquid ligament pointing to the left from the apex of the crescent shaped droplet, see arrow at time $t = 6.2\ \mu s$. This splash has been noted before.[29] The x-ray imaging technique here allows connecting this splash with jetting from secondary cavitation bubbles close to the droplet surface, i.e., between $t = 2.7$ and $t = 3.6\ \mu s$. Bubbles, collapsing near an air–liquid interface, are known to form these so-called Worthington jets.[30]

As the main cavity opens, the surrounding liquid is further stretched and eventually breaks up, see, for example, $t = 18.7\ \mu s$, where on the left part, the liquid film appears still intact, while in the middle and right part of the image, it has already broken up into filaments that further pinch off into droplets. We can identify three temporal regimes in Fig. 3: Initially, sub micrometer-sized droplets are produced during the violent initial dynamics due to the phase explosion, indicated with the arrow at $t = 0.9\ \mu s$. Then, micrometer sized fragments are ejected from the rim at the back of the expanding liquid film, see arrow at $t = 1.8\ \mu s$. At the later stage, larger droplets are formed as a result of the rupture of the liquid film leaving behind ligaments that break up due to the Rayleigh–Plateau instability, see arrow at $t = 18.7\ \mu s$.

Prior to the ejection, a structure on the distal part of the droplet is visible, see frame $t = 18.5$ ns. This phase contrast is likely caused by a modulation of the refractive index, which is a function of pressure and temperature. To understand this pattern, we numerically model the temperature increase in the droplet from deposition of laser energy using a ray tracing method, which is suitable for the present droplet size.[31] Figure 4 shows the ray propagation through the droplet for subsequent times. The rays are entering from the left and are refracted at the droplet interface proximal to the laser (t_2), i.e., the droplet acts as a spherical lens. Its focal length is outside the droplet, and most of the ray energy is transmitted (t_3) through the posterior droplet interface. Yet, a small fraction of the ray power is reflected into the droplet. These rays form a funnel-shaped caustic, see F_f and converge finally to a focal region F_m within the droplet, see t_4. Additionally, a secondary focus of lower intensity is formed at t_5 as a result of secondary reflections of the rays. The ray caustics appearing in t_3 and t_4 indicate locally high laser intensities.

In t_4, they are compared to the droplet image, at $t = 18.5$ ns from Fig. 2, in an overlay. The caustics nicely overlap with the structures seen in the experimental frame, thus supporting our hypothesis that laser-induced heating is responsible for the vapor explosion. With this knowledge, we can model the temperature field within the droplet, as shown in Fig. 5.

As a result, the highest temperatures are reached at the focal spot F_m and within the funnel shape in the grayish regions, see Fig. 5(a). There, the critical temperature of water is exceeded. These two sites are

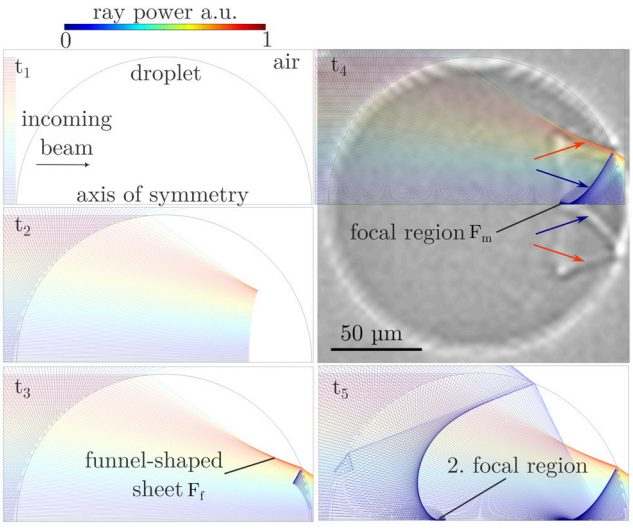

FIG. 4. Ray tracing of the laser beam used for droplet fragmentation for subsequent times $t_1, \ldots, t_5$. The cross section of the upper half of the droplet is shown, and the beam is incoming from the left. The lower horizontal corresponds to the axis of cylindrical symmetry. The ray power is color-coded, where red indicates the highest and dark blue the lowest power in arbitrary units. As each ray represents the power of all rays given by the cylindrical symmetry, rays that are started farther from the optical axis appear red. At the posterior interface of the droplet, a small fraction of the incoming power is reflected. These rays appear blue (t_4) and converge to the focal region F_m. For t_4, an image of the droplet 18.5 ns after the laser pulse is overlaid. It shows a characteristic modulation of index of refraction at the distal side that matches with the funnel shaped ray optic caustic prior reflection at the posterior droplet wall (orange arrows) and after reflection at this wall before reaching the focus F_m (blue arrows).

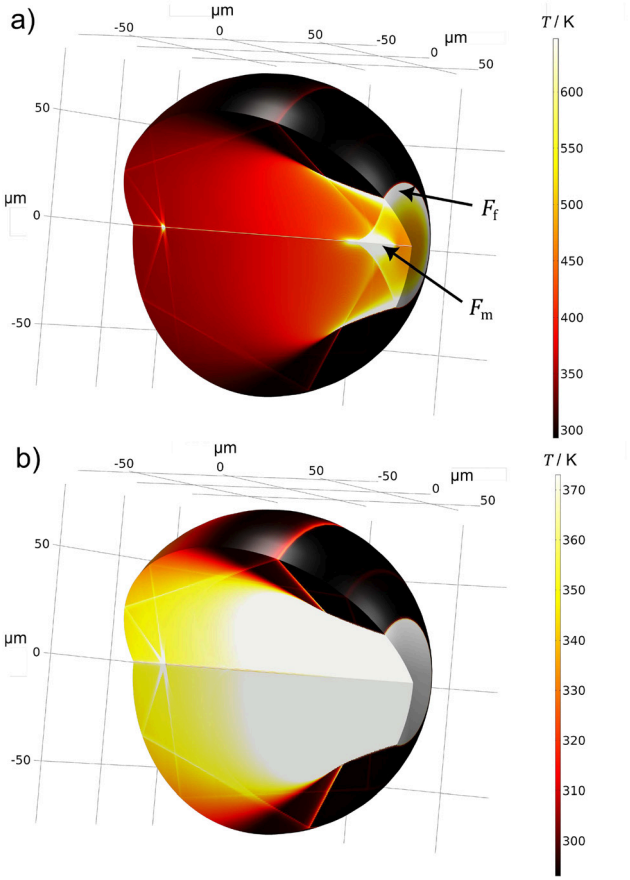

FIG. 5. Temperature distribution in the water droplet of radius $r_d = 75\ \mu m$ from absorption of the laser pulse. The laser is incident from along the x-axis from the left. The color scales are cropped at the critical temperature of water of 647 K in (a) and the boiling temperature of 373 K in (b), i.e., grayish regions in the droplet indicate phase explosion and potential boiling, respectively.

consequently expected to be the locations of phase explosion. Figure 5(b) shows the same view, yet the gray colors indicate temperatures above the boiling temperature. This volume is metastable and prone to a liquid–vapor phase change.

The temperature distribution shown in Fig. 5(b) offers some insight to connect the fragmentation dynamics shown in Fig. 3 with the laser propagation. The gray-colored part of the droplet heated to the critical temperature explosively expands into vapor and ejects it to the posterior droplet side. In contrast, the yellow-colored colder region in Fig. 5(b) on the left is not directly evaporated but remains liquids and moves due to momentum conservation to the left. As a result, these colder upper and anterior parts of the droplet become stretched and fragment into filaments. The main cavity in the droplet is surrounded by a thin liquid layer that corresponds to the unheated (dark) regions outside the funnel-shaped heating region in Fig. 5.

At the second focal region (see Fig. 4 at t_5), another small whitish region is formed in the axial symmetry of the simulation (see Fig. 5), i.e., some phase explosion may be expected here too. However, we do not detect a phase modulation in Fig. 2 at the second focus. This second focus is a result of diffraction and repeated ray reflection at the water/air interface, and probably, slight deviations from the perfect symmetry accumulate and result in a broadened second focus. In addition, the high intensities at the first focal region may produce non-linear effects effectively absorbing the light more than in our linear and static model accounted for, reducing the energy delivered to the second focal region. The refraction geometry of the droplet is self-similar, i.e., the length scale of focal regions of the laser and their location within the droplet scale with r_d.

A. Spray dynamics

In the initial stage of explosive ejection, small droplets are ejected from the laser focus side and the rim of the developing thin liquid sheet, and we see that after about $\approx 5\,\mu$s, liquid ligaments are formed that successively break up into droplets. The velocity and size of this spray, produced at the later stage, can be quantified from the high-speed recordings due to the near infinite depth of focus of the imaging arrangement. An example of the sheet dynamics and resulting spray is shown in Fig. 6(a). Here, the rim of the liquid sheet moves leftward, eventually leaving the field of view. Holes in the sheet appear and subsequently grow, resulting in the formation of filaments ($t = 24$ and $t = 40\,\mu$s). These filaments further fragment by droplet pinch-off. The process resembles the breakup of a thin liquid film subjected to an impulsive acceleration, see, for example, Bremond and Villermaux[32] and Villermaux.[1] There the instability of the liquid film is induced by a Rayleigh–Taylor instability forming holes in the film that expand and result in a "web of liquid ligaments." The later breakup of the corrugated liquid ligament due to capillary destabilization into droplets has been described by Villermaux *et al.*[33] They proposed that this distribution contains droplets that are larger in radius than the ligament radius, and the distribution follows a Γ-function,

$$p(x = R/\langle R\rangle) = \frac{n^n}{\Gamma(n)} x^{n-1} e^{-nx}, \tag{1}$$

where n is a fit parameter. Also, we normalize the droplet radius with the mean droplet radius $\langle R\rangle$. The experimentally obtained distribution of the droplet sizes is given in Fig. 6(b). It shows the probability density function of droplet radii for the time when no more ligaments are seen and no further droplet fragmentation is observed, i.e., during the time interval of 93–114 μs. As fit parameter, a value of $n = 3.94$ is obtained, which is a typical value for corrugated filaments.[1] The droplet mean diameter is $\langle R\rangle = 3.49\,\mu$m, i.e., significantly below of what could be measured in a volumetric spray using optical techniques even with advanced optics and smart image processing algorithms.[34]

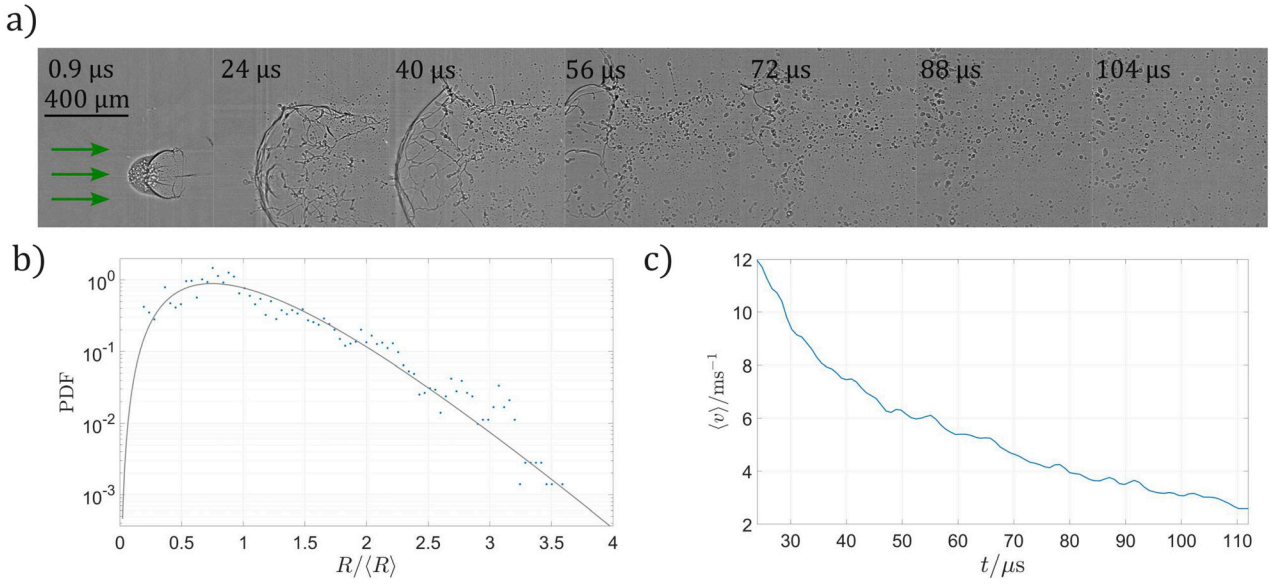

FIG. 6. Spray dynamics and characterization during a later stage when the ligaments are further pinching off. (a) Spray dynamics, please note the larger field of view as compared to Fig. 3. (b) Probability density function of droplet radii and fit using Eq. (1) with $\langle R\rangle = 3.49\,\mu$m and $n = 3.94$. (c) Mean droplet velocity in the spray as a function of time. Please see Fig. 9 for a video of spray evolution and droplet tracking.

The droplet mean velocity $\langle v \rangle$ is about 12 ms^{-1} at $t = 24\,\mu$s and decreases for later times as the faster droplet moves out of the imaging section, see Fig. 6(c). From droplet sizes and their velocities, in addition, the total surface energy $E_\sigma = \sum_{i=1}^{N} 4\pi R_i^2 \sigma$ and kinetic energy $E_{\text{kin}} = \sum_{i=1}^{N} 4/3\pi R_i^3 \rho v^2$ can be estimated, where R_i and v_i are the radius and velocity of the ith droplet and σ and ρ are the coefficient of surface tension and the specific mass density of water, respectively, and the sum is taken over all N particles in the frame. To study the spray, we only consider round droplets and exclude filaments from the evaluation as described in Sec. II, and average over the time interval 56–72 μs, that is when the spray is almost fully formed, but the faster droplets are still within the imaging section, and find $E_\sigma = 3.01$ nJ and $E_{\text{kin}} = 3.96$ nJ, i.e., both energy forms are of similar value within the spray.

A measure for the symmetry of fragmentation is the relative net momentum associated with the spray in the x- and y-directions, respectively, $p^{x|y} = \sum_{i=1}^{N} v_i^{x|y} 4/3\pi R_i^3 \rho / \sum_{i=1}^{N} \sqrt{v_i^{x2} + v_i^{y2}}) 4/3\pi R_i^3 \rho$, which should be zero for an ideally symmetric dynamics. We evaluate the droplet momentum only within a section symmetric around the initial droplet and find averaged over $t = 0 - 114\,\mu$s, i.e., over all times of the imaging series, $p^x = 1.3\%$ and $p^y = 3.4\%$. This implies indeed a good approximation of symmetric fragmentation.

IV. CONCLUSIONS

Megahertz x-ray microscopy of explosive laser-induced droplet fragmentation offered an unprecedented look into the droplet just prior and after the phase explosion that would have not been possible with visible light. As a result, two distinct mechanisms of phase transition and thus of atomization are revealed: (1) the localized heating of the droplet above the critical temperature resulting in a phase explosion and (2) the nucleation of homogeneous cavitation, likely from shockwave reflection at the liquid–gas boundaries. The morphology of the non-homogeneously, axisymmetrically heated region agrees well with the optical caustics within the droplet. The virtually unlimited depth of field enabled the in-focus imaging of the sheet breakup and filament dynamics, supporting a breakup scenario proposed by Villermaux *et al.*[33] With the megahertz x-ray microscopy setup, the fragmentation process of droplets can be elucidated where visible light has met its limits, e.g., for microscopic multi-component droplets and droplets of liquid metals.

ACKNOWLEDGMENTS

We thank Katja Guttmann from University Magdeburg for help with the nozzle preparation and tubing. We acknowledge Henry Chapman for his discussions and suggestions. This work was supported by the internal EuXFEL R&D project: MHz X-ray Microscopy, 2020-2022, and the HORIZON-EIC-2021-PATHFINDEROPEN-01-01, MHz-TOMOSCOPY project, Grant No. 101046448. We acknowledge SPB/SFX instrument for providing internal measurement time for this project.

AUTHOR DECLARATIONS

Conflict of Interest

The authors have no conflicts to disclose.

Author Contributions

Fabian Reuter: Conceptualization (lead); Data curation (equal); Formal analysis (equal); Investigation (lead); Methodology (lead); Project administration (equal); Validation (equal); Visualization (lead); Writing – original draft (lead); Writing – review & editing (equal). **Tokushi Sato:** Investigation (equal); Methodology (equal). **Valerio Bellucci:** Investigation (equal); Methodology (equal). **Sarlota Birnsteinova:** Investigation (equal); Methodology (equal). **Carsten Deiter:** Investigation (equal); Methodology (equal). **Jayanath C. P. Koliyadu:** Methodology (equal). **Romain Letrun:** Methodology (equal). **Pablo Villanueva-Perez:** Investigation (equal). **Richard Bean:** Methodology (equal). **Adrian Mancuso:** Methodology (equal). **Alke Meents:** Methodology (equal). **Patrik Vagovic:** Conceptualization (equal); Funding acquisition (lead); Investigation (equal); Methodology (equal). **Claus-Dieter Ohl:** Conceptualization (equal); Investigation (equal); Validation (equal); Writing – review & editing (lead).

DATA AVAILABILITY

The data that support the findings of this study are available within the article.

APPENDIX: ACOUSTIC TRAPPING OF THE DROPLETS

Here, by generating a spray, a huge span of initial conditions, i.e., combinations between droplet size and velocities, is realized. This way, some droplets in the spray perfectly match the conditions

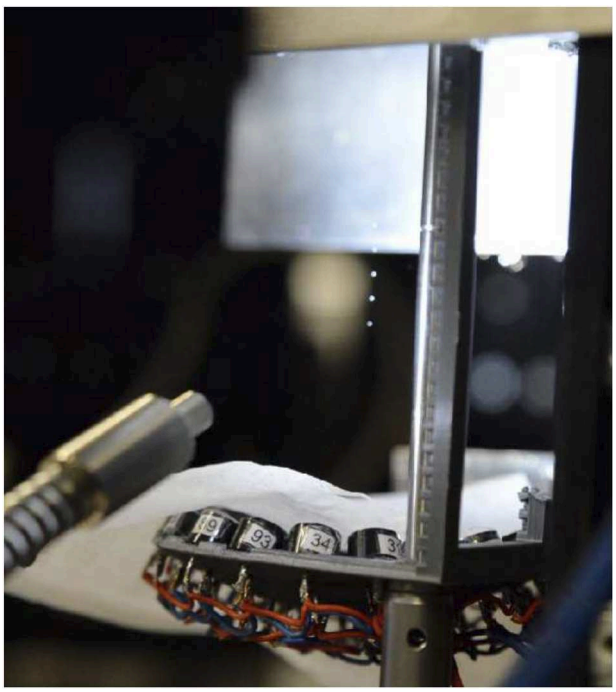

FIG. 7. Photograph of five stable water droplets along a line (interdroplet distance $\lambda/2 \approx 8.6$ mm) in the acoustic levitator. The lower levitator dish with some acoustic transducers and electrical connections on the backside is also visible.

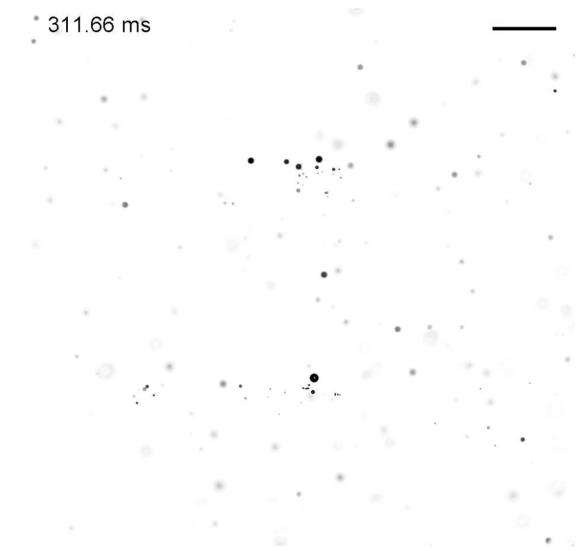

FIG. 8. View of the spray from which a droplet is trapped for further study. The spray is incident from the right. Once the nozzle has been closed for some time, the predominant droplet velocity is in the vertical direction owed to gravity ($t \gtrapprox 200$ ms). In the range of 200 ms $\lessapprox t \gtrapprox$ 400 ms, the trapped droplets grow via coalescence. Toward the end of the video sequence, two droplets are trapped and separated by half of the acoustic wavelength. Once the airflow from the spray generation has completely decayed, which is the case after a few seconds, one of the droplets is chosen for further study and fragmented using a laser pulse. Times stamps in the movie are given with respect to the first frame of the series, exposure time 1.25 μs, and the scale bar corresponds to 1 mm. Multimedia available online.

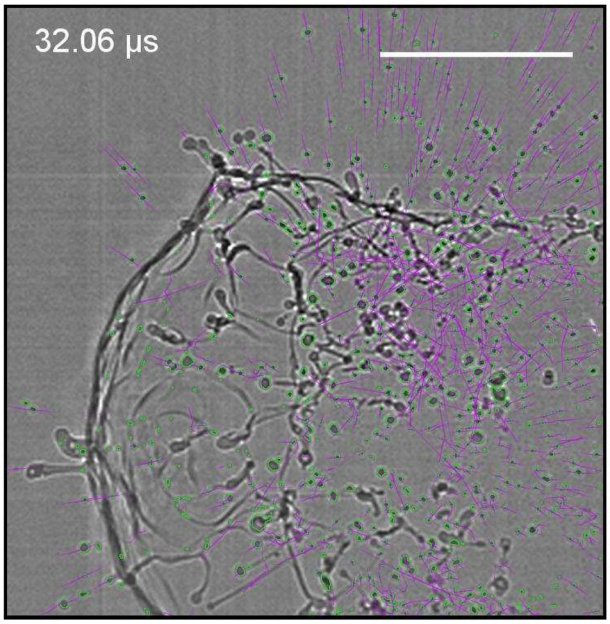

FIG. 9. A video of the droplet fragmentation of Fig. 3 as well as Fig. 6. The scale bar corresponds to 250 μm. For times $t > 26$ μs, the spray is quantitatively characterized, identified droplets are indicated in green, and their tracks of motion are indicated by the magenta colored lines. Please note that droplets identified in less than five subsequent frames are discarded from the data evaluation. Multimedia available online.

for acoustic trapping. This "statistical" spray approach to prepare single droplets was found beneficial in our automatic droplet trapping setup, as it circumvents many complications that we encountered in pretests using precise single droplet generation. For example, employing a droplet generator required a precise alignment of the droplet injection position, angle, and droplet ejection velocity with respect to the sound field. This alignment at the desired low acoustic intensities is very sensitive and would require continuous re-adjustment to account for thermal drift of the acoustic resonator or varying air flow in the experimental chamber. An example of droplets in successive nodes of the acoustic trap is shown in Fig. 7. A high-speed movie of the droplet trapping in the acoustic field is available online, see the snapshot in Fig. 8.

REFERENCES

[1]E. Villermaux, "Fragmentation," Annu. Rev. Fluid Mech. **39**, 419–446 (2007).
[2]A. L. Klein, D. Kurilovich, H. Lhuissier, O. O. Versolato, D. Lohse, E. Villermaux, and H. Gelderblom, "Drop fragmentation by laser-pulse impact," J. Fluid Mech. **893**, A7 (2020).
[3]L. Biasiori-Poulanges and H. El-Rabii, "Shock-induced cavitation and wavefront analysis inside a water droplet," Phys. Fluids **33**, 097104 (2021).
[4]J. Field, J.-J. Camus, M. Tinguely, D. Obreschkow, and M. Farhat, "Cavitation in impacted drops and jets and the effect on erosion damage thresholds," Wear **290–291**, 154–160 (2012).
[5]A. Lindinger, J. Hagen, L. D. Socaciu, T. M. Bernhardt, L. Wöste, D. Duft, and T. Leisner, "Time-resolved explosion dynamics of H_2O droplets induced by femtosecond laser pulses," Appl. Opt. **43**, 5263–5269 (2004).
[6]S. R. G. Avila and C.-D. Ohl, "Fragmentation of acoustically levitating droplets by laser-induced cavitation bubbles," J. Fluid Mech. **805**, 551–576 (2016).
[7]D. Rao, A. P. Singh, and S. Basu, "Laser-induced deformation and fragmentation of droplets in an array," Int. J. Multiphase Flow **148**, 103925 (2022).
[8]V. S. Jagadale, D. C. K. Rao, D. Deshmukh, D. Hanstorp, and Y. N. Mishra, "Modes of atomization in biofuel droplets induced by a focused laser pulse," Fuel **315**, 123190 (2022).
[9]C. A. Stan, D. Milathianaki, H. Laksmono, R. G. Sierra, T. McQueen, M. Messerschmidt, G. J. Williams, J. E. Koglin, T. J. Lane, M. Hayes, S. A. H. Guillet, M. Liang, A. L. Aquila, P. R. Willmott, J. Robinson, K. L. Gumerlock, S. Botha, K. Nass, I. Schlichting, R. Shoeman, H. A. Stone, and S. Boutet, "Liquid explosions induced by x-ray laser pulses," Nat. Phys. **12**, 966–971 (2016).
[10]D. Kurilovich, T. de Faria Pinto, F. Torretti, R. Schupp, J. Scheers, A. S. Stodolna, H. Gelderblom, K. S. Eikema, S. Witte, W. Ubachs *et al.*, "Expansion dynamics after laser-induced cavitation in liquid tin microdroplets," Phys. Rev. Appl. **10**, 054005 (2018).
[11]D. Kurilovich, "Laser-induced dynamics of liquid tin microdroplets," Ph.D. thesis (Vrije Universiteit Amsterdam, 2019).
[12]S. Y. Grigoryev, B. V. Lakatosh, M. S. Krivokorytov, V. V. Zhakhovsky, S. A. Dyachkov, D. K. Ilnitsky, K. P. Migdal, N. A. Inogamov, A. Y. Vinokhodov, V. O. Kompanets, Y. V. Sidelnikov, V. M. Krivtsun, K. N. Koshelev, and V. V. Medvedev, "Expansion and fragmentation of a liquid-metal droplet by a short laser pulse," Phys. Rev. Appl. **10**, 064009 (2018).
[13]M. Krivokorytov, Q. Zeng, B. Lakatosh, A. Y. Vinokhodov, Y. V. Sidelnikov, V. Kompanets, V. Krivtsun, K. Koshelev, C. Ohl, and V. Medvedev, "Shaping and controlled fragmentation of liquid metal droplets through cavitation," Sci. Rep. **8**, 597 (2018).
[14]Z. Wang, T. Hopfes, M. Giglmaier, and N. A. Adams, "Experimental investigation of shock-induced tandem droplet breakup," Phys. Fluids **33**, 012113 (2021).
[15]S. Grigoryev, B. Lakatosh, P. Solyankin, M. Krivokorytov, V. Zhakhovsky, S. Dyachkov, C.-D. Ohl, A. Shkurinov, and V. Medvedev, "Jet effusion from a metal droplet irradiated by a polarized ultrashort laser pulse," Phys. Rev. Appl. **18**, 024072 (2022).
[16]L. Biasiori-Poulanges and K. Schmidmayer, "A phenomenological analysis of droplet shock-induced cavitation using a multiphase modeling approach," Phys. Fluids **35**, 013312 (2023).

[17]R. Forehand, K. Nguyen, C. Anderson, R. Shannon, S. Grace, and M. Kinzel, "A numerical assessment of shock–droplet interaction modeling including cavitation," Phys. Fluids **35**, 023315 (2023).
[18]Q. Zeng, S. R. Gonzalez-Avila, S. T. Voorde, and C.-D. Ohl, "Jetting of viscous droplets from cavitation-induced Rayleigh-Taylor instability," J. Fluid Mech. **846**, 916–943 (2018).
[19]P. Vagovič, T. Sato, L. Mikeš, G. Mills, R. Graceffa, F. Mattsson, P. Villanueva-Perez, A. Ershov, T. Faragó, J. Uličný, H. Kirkwood, R. Letrun, R. Mokso, M.-C. Zdora, M. P. Olbinado, A. Rack, T. Baumbach, A. Meents, H. N. Chapman, and A. P. Mancuso, "Megahertz x-ray microscopy at x-ray free-electron laser and synchrotron sources," Optica **6**, 1106–1109 (2019).
[20]M. Pergament, G. Palmer, M. Kellert, K. Kruse, J. Wang, L. Wissmann, U. Wegner, M. Emons, D. Kane, G. Priebe *et al.*, "Versatile optical laser system for experiments at the European x-ray free-electron laser facility," Opt. Express **24**, 29349–29359 (2016).
[21]G. Palmer, M. Kellert, J. Wang, M. Emons, U. Wegner, D. Kane, F. Pallas, T. Jezynski, S. Venkatesan, D. Rompotis *et al.*, "Pump–probe laser system at the FXE and SPB/SFX instruments of the European x-ray free-electron laser facility," J. Synchrotron Radiat. **26**, 328–332 (2019).
[22]A. Marzo, A. Barnes, and B. W. Drinkwater, "TinyLev: A multi-emitter single-axis acoustic levitator," Rev. Sci. Instrum. **88**, 085105 (2017).
[23]J.-Y. Tinevez, N. Perry, J. Schindelin, G. M. Hoopes, G. D. Reynolds, E. Laplantine, S. Y. Bednarek, S. L. Shorte, and K. W. Eliceiri, "Trackmate: An open and extensible platform for single-particle tracking," Methods **115**, 80–90 (2017).
[24]G. Abbate, U. Bernini, E. Ragozzino, and F. Somma, "The temperature dependence of the refractive index of water," J. Phys. D **11**, 1167 (1978).
[25]K. A. Nugent, D. Paganin, and T. E. Gureyev, "A phase odyssey," Phys. Today **54**(8), 27–32 (2001).
[26]Y. Liu, J. Nelson, C. Holzner, J. Andrews, and P. Pianetta, "Recent advances in synchrotron-based hard x-ray phase contrast imaging," J. Phys. D **46**, 494001 (2013).
[27]J. Padilla-Martinez, C. Berrospe-Rodriguez, G. Aguilar, J. Ramirez-San-Juan, and R. Ramos-Garcia, "Optic cavitation with CW lasers: A review," Phys. Fluids **26**, 122007 (2014).
[28]K. Schmidmayer and L. Biasiori-Poulanges, "Geometry effects on the droplet shock-induced cavitation," Phys. Fluids **35**, 063315 (2023).
[29]S. T. Thoroddsen, K. Takehara, T. Etoh, and C.-D. Ohl, "Spray and microjets produced by focusing a laser pulse into a hemispherical drop," Phys. Fluids **21**, 112101 (2009).
[30]S. Gekle and J. M. Gordillo, "Generation and breakup of Worthington jets after cavity collapse. Part 1. Jet formation," J. Fluid Mech. **663**, 293–330 (2010).
[31]W. J. Glantschnig and S.-H. Chen, "Light scattering from water droplets in the geometrical optics approximation," Appl. Opt. **20**, 2499–2509 (1981).
[32]N. Bremond and E. Villermaux, "Bursting thin liquid films," J. Fluid Mech. **524**, 121–130 (2005).
[33]E. Villermaux, P. Marmottant, and J. Duplat, "Ligament-mediated spray formation," Phys. Rev. Lett. **92**, 074501 (2004).
[34]T. Kamiya, M. Asahara, T. Yada, K. Mizuno, and T. Miyasaka, "Study on characteristics of fragment size distribution generated via droplet breakup by high-speed gas flow," Phys. Fluids **34**, 012118 (2022).